Objective Vortex Corelines of Finite-sized Objects in Fluid Flows

Tobias Günther and Holger Theisel

Abstract— Vortices are one of the most-frequently studied phenomena in fluid flows. The center of the rotating motion is called the vortex coreline and its successful detection strongly depends on the choice of the reference frame. The optimal frame moves with the center of the vortex, which incidentally makes the observed fluid flow steady and thus standard vortex coreline extractors such as Sujudi-Haimes become applicable. Recently, an objective optimization framework was proposed that determines a near-steady reference frame for tracer particles. In this paper, we extend this technique to the detection of vortex corelines of inertial particles. An inertial particle is a finite-sized object that is carried by a fluid flow. In contrast to the usual tracer particles, they do not move tangentially with the flow, since they are subject to gravity and exhibit mass-dependent inertia. Their particle state is determined by their position and own velocity, which makes the search for the optimal frame a high-dimensional problem. We demonstrate in this paper that the objective detection of an inertial vortex coreline can be reduced in 2D to a critical point search in 2D. For 3D flows, however, the vortex coreline criterion remains a parallel vectors condition in 6D. To detect the vortex corelines we propose a recursive subdivision approach that is tailored to the underlying structure of the 6D vectors. The resulting algorithm is objective, and we demonstrate the vortex coreline extraction in a number of 2D and 3D vector fields.

Index Terms—Vortex extraction, inertial particles, objectivity, vortex coreline

◆

1 INTRODUCTION

Vortical motion is a key aspect of fluid dynamical processes and is highly relevant to describe and understand many natural flow phenomena. In flow visualization as well as in other disciplines, an overwhelming amount of research has been devoted to define, extract and visualize vortices [31]. Despite these efforts, the search for new and better vortex concepts remains an active field of ongoing research. Initiated by Haller [32], the search for *objective* vortex measures shifted back into focus. Objective measures guarantee a highly desirable property: they are invariant under smooth rotations and translations of the reference frame. This means, the vortex measure delivers the same result in any arbitrarily moving reference frame. This allows for a clear and unambiguous definition of vortices, which is especially challenging in time-dependent flows. Incidentally, objectivity has another important consequence [22]: since the movement of the observer and the movement of the vortex are relative to each other, an objective method can also robustly detect vortices that are moving on any translating and/or rotating path. All existing objective vortex concepts were developed for non-inertial flows, i.e., the movement of massless particles that move tangentially with the flow.

In this work, we concentrate on the vortical motion of finite-sized objects that are immersed in a fluid flow, for which Günther and Theisel [25] have shown that the center of the vortex is mass-dependent. These so-called *inertial* particles are a central element in many scientific problems, such as sand saltation modeling [64], soiling of cars [55], formation of rain [7], jellyfish feeding [50, 60] and spacecraft navigation [65]. Vortex structures are similarly relevant in the inertial case, for instance during the uplift of dust and sand during helicopter landing maneuvers [42, 70, 71] or for the detection of marine debris and plankton species in the oceans [39]. Same as in the massless case, objectivity is desirable for the vortex detection of inertial particles. However, to the best of our knowledge, no objective vortex concepts exist for inertial flows yet. At present, the highest class of reference frame invariance for inertial particle motion is Galilean invariance [25], which is the invariance under reference frame translations with constant speed in a constant direction. Objective vortex concepts cannot straightforwardly be extended from the massless case, since they depend on both the particle's mass and the particle's own velocity. This own velocity unfortunately changes when observing the flow in a different reference frame, turning the extraction into a high-dimensional problem.

In this paper, we introduce the first approach to extract and visualize the corelines of objective vortices in inertial flows. For this, we make use of an important observation that was made for massless flows [22]: vortex measures become automatically objective, if they are observed in a reference frame that moves with the vortex [53] and in which the observed flow incidentally becomes steady [43]. By describing the inertial particle motion in a high-dimensional non-inertial flow, i.e., as a coupled first-order ODE, we derive a linear optimization based on [22] for the extraction of the optimal as-steady-as-possible reference frame of inertial particles. Once the frame is found, we apply vortex coreline extractors in the high-dimensional flow. If the underlying flow is two-dimensional, the search for inertial vortex centers gracefully reduces to a critical point search in 2D, which is very efficient. Our definition of vortex corelines in 3D is based on the Sujudi-Haimes [69] method, which can be rephrased using the parallel vectors operator [49]. Unfortunately, the high-dimensional parallel vectors formulation does not simply reduce back to 3D. Instead, an expensive parallel vectors search in the full 6D space is required, for which we formulate a recursive Bezier-based subdivision approach. Aside from being invariant under more general motions, our objective algorithm is much more robust than the Galilean invariant method of Günther and Theisel [25]. However, the higher reference frame invariance and the superior extraction results are bought at the expense of a much higher computational cost, since a 6D parallel vectors search is for numerical flows in the order of hours. We apply our inertial vortex coreline extraction algorithm in multiple time-dependent 2D and 3D vector fields.

First, we discuss different classes of reference frame invariance, existing vortex extraction algorithms for tracer particles and related work on inertial particles in Section 2. In Section 3, we give a concise summary of our objective vortex coreline extraction algorithm for inertial particles in 2D and 3D. Afterwards, we derive and analyze our method in detail in Section 4, with implementation details in Section 5. Subsequently, the algorithms are applied in Section 6 in several 2D and 3D flows, which is followed by a conclusion in Section 7.

Notation

For notational convenience, we introduce the subscript p to denote a multiplication with the Levi-Civita symbol: $\mathbf{x}_p = \varepsilon_{ij[k]}\mathbf{x}$, which rotates a vector (in 2D) or transforms it to an anti-symmetric matrix (in 3D):

$$\text{in 2D: } \mathbf{x}_p = \begin{pmatrix} -y \\ x \end{pmatrix} \quad \text{in 3D: } \mathbf{x}_p = \begin{pmatrix} 0 & -z & y \\ z & 0 & -x \\ -y & x & 0 \end{pmatrix} \quad (1)$$

• *Tobias Günther is with the Computer Graphics Laboratory at ETH Zürich. E-mail: tobias.guenther@inf.ethz.ch.*
• *Holger Theisel is head of the Visual Computing Group at University of Magdeburg. E-mail: theisel@ovgu.de.*

We use function ap [22] that transforms an anti-symmetric matrix $\mathbf{M} = (m_{i,j})$ to a scalar/vector. In 2D, $ap(\mathbf{M}) = \frac{1}{2}(m_{1,2} - m_{2,1})$, and in 3D, $ap(\mathbf{M}) = \frac{1}{2}(m_{3,2} - m_{2,3}, m_{1,3} - m_{3,1}, m_{2,1} - m_{1,2})^{\mathrm{T}}$. We denote the zero vector as $\mathbf{0}$, the zero matrix as $\mathbf{0}_{n \times n}$ and the identity matrix as $\mathbf{I}$. Later, we denote temporal derivatives as $\dot{\mathbf{Q}} = \frac{d\mathbf{Q}(t)}{dt}$ and $\ddot{\mathbf{Q}} = \frac{d^2\mathbf{Q}(t)}{dt^2}$

2 RELATED WORK

Despite decades of research in scientific visualization, fluid dynamics and continuum mechanics, feature extraction in time-dependent flows remained a challenging problem [31], since the choice of the reference frame greatly influences the extraction of features such as vortices [43, 53]. This led to two different approaches:

1. Extraction methods that give the same result for certain types of reference frame motions [32, 37, 38, 79].

2. The search for an optimal reference frame, in which vortices appear [6, 22].

In the following, we discuss both approaches in more detail and afterwards explain the visualization of finite-sized objects in fluids.

2.1 Reference Frame Invariance

There are two main classes of reference frame invariance.

Galilean Invariance. A measure that is invariant under reference frames that move with constant speed in a constant direction is Galilean invariant. Incidentally, such a vortex measure can find vortices that translate with constant speed in a constant direction. Most region-based vortex measure that are used in practice are Galilean invariant, such as the Δ-criterion of Chong et al. [11], the λ_2-criterion by Jeong and Hussain [38], the Q-criterion of Hunt [37], vorticity ω, and the Okubo-Weiss criterion [47, 80]. By considering the domain in polar coordinates, Galilean invariant methods become rotation invariant [24].

Objectivity. In continuum mechanics [32], a measure is called objective, if it is does not change under any smooth rotation and translation of the reference frame. Such a moving frame transforms a point $(\mathbf{x}, t)$ in space-time to a new location $(\mathbf{x}^*, t^*)$ by

$$\mathbf{x}^* = \mathbf{Q}(t)\,\mathbf{x} + \mathbf{c}(t) \quad , \quad t^* = t - a \qquad (2)$$

with the time-dependent rotation matrix $\mathbf{Q}(t) \in SO(3)$, the time-dependent translation vector $\mathbf{c}(t)$, and constant a. Objectivity can be formalized, cf. Truesdell [77]:

Definition 1 *A scalar s is objective if it remains unchanged under any change of the reference frame as in Eq.* (2). *A vector* $\mathbf{r}$ *is objective if Eq.* (2) *transforms it to* $\mathbf{r}^* = \mathbf{Q}(t)\mathbf{r}$. *A second-order tensor* $\mathbf{T}$ *is objective if Eq.* (2) *transforms it to* $\mathbf{T}^* = \mathbf{Q}(t)\mathbf{T}\mathbf{Q}(t)^{\mathrm{T}}$.

2.2 Vortex Corelines

Next, we introduce vortex coreline extractors of massless particles, following the categorization of Günther and Theisel [31].

Corelines in Steady Flow. Helman and Hesslink [35] located vortex centers as critical points $\mathbf{u} = \mathbf{0}$ with complex eigenvalues in the Jacobian. For 3D flows, Globus et al. [19] computed swirling critical points and traced streamlines in the direction of the eigenvector with corresponding real-valued eigenvalue. The reduced velocity criterion of Sujudi and Haimes [69] finds locations at which the flow vector $\mathbf{u}$ is parallel to the eigenvector with corresponding real-valued eigenvalue. This method found numerous applications [18, 40]. Peikert and Roth [49] used the parallel vectors operator to rephrase this approach to $\mathbf{u} \parallel \mathbf{J}\mathbf{u}$ and extended the method to handle bent vortex corelines [56].

Corelines in Unsteady Flow. Early approaches for unsteady flow tracked cores of swirling streamlines over time, e.g., Bauer and Peikert [4], Tricoche et al. [76] and Theisel et al. [73]. This, however, is only useful when studying instantaneous fields such as magnetic fields. Weinkauf et al. [79] and Fuchs et al. [16] developed techniques for unsteady flows by either considering the swirling motion in space-time [79] or by using the unsteady acceleration in the parallel vectors form of Sujudi-Haimes [16].

Extremum Lines. A number of vortex coreline methods have been defined as extremal structures of region-based approaches, including minimum lines of pressure [46] and maximum lines of vorticity magnitude [67]. As shown by Peikert and Roth [49], many criteria can be formulated with the parallel vectors operator, including extremal lines of the normalized helicity. Using feature flow fields [74], Sahner et al. [58] traced extremum lines of λ_2 and Q. Later, Sahner et al. [59] extracted extremal structures of Q [37] and the M_z-criterion [32] to compute vortex and strain skeletons. The topology of λ_2-based extremal structures was further studied by Schafhitzel et al. [63]. For a general discussion of extremal structures, see Kindlmann et al. [41].

2.3 Objective Vortex Methods

Next, we revisit objective regions-based methods for massless particles.

Relative Vorticity Tensor-based Measures. The anti-symmetric part of the Jacobian is called vorticity tensor. It captures the local rotation behavior, but is only Galilean invariant. By viewing this tensor in the objective strain basis, Drouot and Lucius [14], and Dresselhaus, Tabor and Klapper [13, 72] derived an objective counterpart: the *relative vorticity tensor*. Its objectivity was proven by Astarita [1], who also defined an index measure that distinguishes between extension-like motions and rigid-body-like rotations. By using the relative vorticity, standard measures such as λ_2 and Q become objective [32, 44, 75].

Strain Tensor-based Measures. Unlike the vorticity tensor, the symmetric part of the Jacobian is objective. Based on the strain-rate tensor, Haller [32] proposed the M_z criterion for incompressible flows. His approach marks regions of non-hyperbolic particle behavior, i.e., elliptic regions. With the assumption that vortices stay coherent over time, the long-term residence of a particle in an elliptic region is taken as indicator for a vortex.

Vorticity-based Measures. Vorticity itself is only Galilean invariant, cf. [1, 33], but its spatial derivatives and extrema are objective [67]. By subtracting the average vorticity in the local neighborhood, Haller et al. [33] introduced the instantaneous vorticity deviation (IVD). Integrating this measure along trajectories produces the Lagrangian-averaged vorticity deviation (LAVD). Both IVD and LAVD depend on the chosen neighborhood size, making their value range relative to it, i.e., these quantities do not directly translate to (half) the angular speed of the rotation. Robinson [53] pointed out that vorticity can produce false positives in shear flow, which might require post-processing.

To the best of our knowledge, there are no objective measures that are applicable to inertial flows.

2.4 Inertial Particles

Inertial Particle Motion. When considering particles with a finite size, their trajectories are influenced by inertia and gravity. The most accurate description of the motion of spherical objects in fluids goes back to the seminal work of Maxey and Riley [45], see Farazmand and Haller [15] for a recent review. Often, the equations of motion are simplified by placing application-specific assumptions. These include small particle sizes, a high particle density compared to the surrounding medium and disregarding both two-way coupling and particle collisions. These simplifications are frequently made [5, 10, 42, 51, 70] and lead to the following equation of motion, cf. Crowe et al. [12].

For an unsteady n-D velocity field $\mathbf{u}(\mathbf{x}, t)$ with $n \in \{2, 3\}$ and the Jacobian $\mathbf{J} = \nabla \mathbf{u}$, the state of an inertial particle $\tilde{\mathbf{x}} = (\mathbf{x}, \mathbf{v})^{\mathrm{T}}$ with position $\mathbf{x}$ and velocity $\mathbf{v}$ evolves over time according to the $2n$-D vector field:

$$\tilde{\mathbf{u}}(\tilde{\mathbf{x}}, t) = \tilde{\mathbf{u}}(\mathbf{x}, \mathbf{v}, t) = \begin{pmatrix} \mathbf{v} \\ \frac{\mathbf{u}(\mathbf{x},t) - \mathbf{v}}{r} + \mathbf{g} \end{pmatrix} \quad \text{with} \quad r = \frac{d_p^2\,\rho_p}{18\,\mu} . \qquad (3)$$

The above equation is parameterized by the *response time* r, which comprises particle diameter d_p, particle density ρ_p and the viscosity of the surrounding air μ. The gradient and the temporal derivative are:

$$\tilde{\mathbf{J}} = \nabla \tilde{\mathbf{u}} = \begin{pmatrix} \mathbf{0}_{n \times n} & \mathbf{I} \\ \frac{1}{r}\mathbf{J} & -\frac{1}{r}\mathbf{I} \end{pmatrix} \quad \text{and} \quad \tilde{\mathbf{u}}_t = \begin{pmatrix} \mathbf{0} \\ \frac{1}{r}\mathbf{u}_t \end{pmatrix} . \qquad (4)$$

Visualization of Inertial Particles. The study of inertial particle motion is a relatively young field in the visualization community. In an early work, Roettger et al. [55] visualized the soiling of cars via heat maps before the cars were manufactured. Günther et al. extended several visualization concepts to the inertial case, including integral geometry [23], separation behavior [26], steady vector field topology [21, 27] and Galilean invariant vortex corelines [25]. In the latter, they applied Sujudi-Haimes to the high-dimensional 2n-D flow, which eventually reduced to an n-D parallel vectors problem. In the high-dimensional phase space, inertial particles are attracted by a slow manifold. Haller [34] calculated the asymptotic velocity, and defined an ODE for the movement on the manifold. Baeza Rojo et al. [3] used multiple coordinated views to visualize heterogeneous mixtures of inertial particles and their interaction with the attracting manifold. Günther and Theisel [28, 29] developed additional techniques for inertial backward integration, which were applied to the calculation of attracting material lines [30]. Hyperbolic inertial Lagrangian coherent structures (ILCS) have also been identified in [50, 61]. Sudharsan et al. [68] observed Lagrangian coherent structures of tracer particles in the context of preferential particle settling. Inertial finite-time Lyapunov exponents were not only calculated based on spatial separation, but also on the separation in the spatio-velocity domain [17] or its subspaces [57].

3 INERTIAL OBJECTIVE VORTICES IN A NUTSHELL

For the inertial particle model in Crowe et al. [12], the motion of a finite-sized object is dependent on the underlying n-D air flow $\mathbf{u}(\mathbf{x},t)$ with Jacobian $\mathbf{J}$ and temporal derivative $\mathbf{u}_t$, gravity $\mathbf{g}$ and particle response time r. First, we briefly summarize the main steps of our extraction algorithm in form of a recipe, since the computation of objective vortex corelines of inertial particles follows a sequence of steps, including the computation of a reference frame in which the high-dimensional flow becomes steady and the subsequent feature extraction. The explanation and the detailed derivation follow later in Section 4. For each point $\mathbf{x}$ on a discrete grid, covering the spatial domain:

1. Compute system matrix $\mathbf{M}$ for particle velocity $\mathbf{v} = \mathbf{0}$, which linearly separates the flow properties from the reference frame:

$$\mathbf{M} = \frac{1}{r}\left(-\mathbf{J}\mathbf{x}_p + \mathbf{u}_p\,,\,\mathbf{J}\,,\,\mathbf{x}_p\,,\,-\mathbf{I}\,,\,\mathbf{0}_p\,,\,\mathbf{0}_{n\times n}\right)$$
$$+ \left(\mathbf{g}_p\,,\,\mathbf{0}_{n\times n}\,,\,2\mathbf{v}_p\,,\,\mathbf{0}_{n\times n}\,,\,\mathbf{x}_p\,,\,-\mathbf{I}\right) \quad (5)$$

2. After summing in a neighborhood region U, solve a linear problem to obtain vector $\mathbf{p}$, containing the reference frame parameters:

$$\widehat{\mathbf{M}}\mathbf{p} = \widehat{\mathbf{y}} \quad (6)$$

$$\text{with} \quad \widehat{\mathbf{M}} = \int_U \mathbf{M}^T\mathbf{M}\,dV + \mathbf{E}\,,\quad \widehat{\mathbf{y}} = \int_U \mathbf{M}^T\mathbf{u}_t\,dV \quad (7)$$

and $\mathbf{E}$ is a diagonal matrix with the last $3n - 3$ entries being set to 1. The solution $\mathbf{p} = (ap(\dot{\mathbf{S}}), \dot{\mathbf{d}}, \dots)$ contains parameters $\dot{\mathbf{S}}$ and $\dot{\mathbf{d}}$.

For a 2D flow:

3. Using the obtained $\dot{\mathbf{S}}$ and $\dot{\mathbf{d}}$, repeat steps (1) and (2) for $\mathbf{v} = -\dot{\mathbf{S}}\mathbf{x} - \dot{\mathbf{d}}$, which gives $\mathbf{p} = (ap(\dot{\mathbf{S}}), \dot{\mathbf{d}}, ap(\ddot{\mathbf{S}}), \ddot{\mathbf{d}}, \dots)$ and thus the remaining required reference frame parameters $\ddot{\mathbf{S}}$ and $\ddot{\mathbf{d}}$.

4. To find vortex cores search for critical points in:

$$\frac{\mathbf{u}(\mathbf{x},t) - \mathbf{v}}{r} + \mathbf{g} + 2\dot{\mathbf{S}}\mathbf{v} + (\ddot{\mathbf{S}} + \dot{\mathbf{S}}\dot{\mathbf{S}})\mathbf{x} + \ddot{\mathbf{d}} + \dot{\mathbf{S}}\dot{\mathbf{d}} = \mathbf{0} \quad (8)$$

For a 3D flow:

3. In $\mathbf{p} = (ap(\dot{\mathbf{S}}), \dot{\mathbf{d}}, ap(\ddot{\mathbf{S}}), \ddot{\mathbf{d}}, \dots)$, only $\ddot{\mathbf{d}}$ is linear in $\mathbf{v}$:

$$\ddot{\mathbf{d}} = \ddot{\mathbf{d}}_0 - ap(\mathbf{q})\,\mathbf{v} \quad (9)$$

Linearly solve for $\ddot{\mathbf{d}}_0$ and $\mathbf{q}$ by sampling $\ddot{\mathbf{d}}$ at two more arbitrary $\mathbf{v}$ by repeating steps (1) and (2) twice. Given $\ddot{\mathbf{d}}_0$ and $\mathbf{q}$, the parameter $\ddot{\mathbf{d}}$ can be computed for a given $\mathbf{v}$.

4. To find vortex corelines, extract the locations $(\mathbf{x}, \mathbf{v})$ at which the two 6D vector fields $\tilde{\mathbf{u}}^*$ and $\tilde{\mathbf{w}}^*$ are parallel, i.e., $\tilde{\mathbf{u}}^* \parallel \tilde{\mathbf{w}}^*$ with

$$\tilde{\mathbf{u}}^* = \begin{pmatrix} \mathbf{v} + \mathbf{a} \\ \mathbf{B}\,\mathbf{v} + \mathbf{b} \end{pmatrix}\,,\quad \tilde{\mathbf{w}}^* = \begin{pmatrix} \mathbf{B}\,\mathbf{v} + \mathbf{b} \\ \mathbf{C}\,\mathbf{v} + \mathbf{c} \end{pmatrix} \quad (10)$$

and $\mathbf{a} = \dot{\mathbf{S}}\mathbf{x} + \dot{\mathbf{d}}$, $\quad \mathbf{b} = \frac{\mathbf{u}}{r} + \mathbf{g} + (\ddot{\mathbf{S}} + \dot{\mathbf{S}}\dot{\mathbf{S}})\mathbf{x} + \ddot{\mathbf{d}}_0 + \dot{\mathbf{S}}\dot{\mathbf{d}}$, $\quad \mathbf{B} = 2\dot{\mathbf{S}} - \frac{1}{r}\mathbf{I} - ap(\mathbf{q})$, $\quad \mathbf{H}_1 = \frac{1}{r}\mathbf{J} + \frac{1}{r}\dot{\mathbf{S}} - \dot{\mathbf{S}}\dot{\mathbf{S}} + \ddot{\mathbf{S}}$, $\quad \mathbf{H}_2 = -\frac{1}{r}\mathbf{I} + 2\dot{\mathbf{S}}$, $\mathbf{C} = \mathbf{H}_1 + \mathbf{H}_2\,\mathbf{B}$, and $\quad \mathbf{c} = \mathbf{H}_1\,\mathbf{a} + \mathbf{H}_2\,\mathbf{b}$.

The derivation of the above algorithm and the description of the 6D parallel vectors extraction follow in the next section.

4 DERIVATION AND ANALYSIS

Lugt [43] and Robinson [53] proposed to identify vortices by closed or spiraling streamlines that can be seen in a reference frame, in which the flow field is steady. In this paper, we search for this optimal reference frame for the high-dimensional vector fields of inertial particles. In the following, we derive the algorithm in Section 3 for the objective computation of vortex corelines of inertial particles.

4.1 Reference Frame Transformation for Inertial Particles

When applying a smooth rotation $\mathbf{Q}(t)$ and translation $\mathbf{c}(t)$ as in Eq. (2) to the reference frame of an inertial particle, its position and velocity in the spatio-velocity domain become:

$$\tilde{\mathbf{x}}^* = \begin{pmatrix} \mathbf{Q}\,\mathbf{x} + \mathbf{c} \\ \mathbf{Q}\left(\mathbf{v} + \mathbf{Q}^T\dot{\mathbf{Q}}\,\mathbf{x} + \mathbf{Q}^T\dot{\mathbf{c}}\right) \end{pmatrix}. \quad (11)$$

In addition, we can calculate the high-dimensional tangent vector field $\tilde{\mathbf{u}}^*$ that describes the motion of the inertial particle in the new reference frame. For notational convenience, we first introduce the abbreviations $\dot{\mathbf{S}}$ and $\dot{\mathbf{d}}$, which are the derivatives of the reference frame rotation $\mathbf{Q}$ and translation $\mathbf{c}$ under the inverse reference frame rotation $\mathbf{Q}^T$. Further, we introduce their derivatives by differentiation using the chain rule:

$$\dot{\mathbf{S}} = \mathbf{Q}^T\dot{\mathbf{Q}} \quad (12)$$
$$\ddot{\mathbf{S}} = \dot{\mathbf{Q}}^T\dot{\mathbf{Q}} + \mathbf{Q}^T\ddot{\mathbf{Q}} \quad (13)$$
$$\dddot{\mathbf{S}} = \ddot{\mathbf{Q}}^T\dot{\mathbf{Q}} + 2\dot{\mathbf{Q}}^T\ddot{\mathbf{Q}} + \mathbf{Q}^T\dddot{\mathbf{Q}}\,, \quad (14)$$

where $\dot{\mathbf{S}}$, $\ddot{\mathbf{S}}$, $\dddot{\mathbf{S}}$ are skew symmetric matrices with vanishing main diagonals. Further, we use the following abbreviations for the translations:

$$\dot{\mathbf{d}} = \mathbf{Q}^T\dot{\mathbf{c}} \quad (15)$$
$$\ddot{\mathbf{d}} = \dot{\mathbf{Q}}^T\dot{\mathbf{c}} + \mathbf{Q}^T\ddot{\mathbf{c}} \quad (16)$$
$$\dddot{\mathbf{d}} = \ddot{\mathbf{Q}}^T\dot{\mathbf{c}} + 2\dot{\mathbf{Q}}^T\ddot{\mathbf{c}} + \mathbf{Q}^T\dddot{\mathbf{c}}\,. \quad (17)$$

Then, the transformed high-dimensional tangent vector field $\tilde{\mathbf{u}}^*$ is:

$$\tilde{\mathbf{u}}^* = \begin{pmatrix} \mathbf{Q}\left(\mathbf{v} + \dot{\mathbf{S}}\mathbf{x} + \dot{\mathbf{d}}\right) \\ \mathbf{Q}\left(\frac{\mathbf{u} - \mathbf{v}}{r} + \mathbf{g} + 2\dot{\mathbf{S}}\mathbf{v} + (\ddot{\mathbf{S}} + \dot{\mathbf{S}}\dot{\mathbf{S}})\mathbf{x} + \ddot{\mathbf{d}} + \dot{\mathbf{S}}\dot{\mathbf{d}}\right) \end{pmatrix} \quad (18)$$

The gradient $\tilde{\mathbf{J}}^* = \nabla\tilde{\mathbf{u}}^*$ is a $2n \times 2n$ matrix and contains the partial derivatives with respect to particle position $\mathbf{x}$ and particle velocity $\mathbf{v}$:

$$\tilde{\mathbf{J}}^* = \begin{pmatrix} \mathbf{0}_{n\times n} & \mathbf{I} \\ \mathbf{Q}\left(\frac{1}{r}\mathbf{J} + \frac{1}{r}\dot{\mathbf{S}} - \dot{\mathbf{S}}\dot{\mathbf{S}} + \ddot{\mathbf{S}}\right)\mathbf{Q}^T & \mathbf{Q}\left(-\frac{1}{r}\mathbf{I} + 2\dot{\mathbf{S}}\right)\mathbf{Q}^T \end{pmatrix} \quad (19)$$

4.2 Linearity of Temporal Derivative

Since we search for a reference frame, in which the flow field becomes steady, we are particularly interested in the temporal derivative of the transformed flow $\tilde{\mathbf{u}}^*$. Fortunately, the temporal derivative depends linearly on the reference frame transformation parameters $\mathbf{Q}$ and $\mathbf{c}$:

$$\tilde{\mathbf{u}}_t^* = \begin{pmatrix} \mathbf{0} \\ \mathbf{Q}\left(\frac{1}{r}\mathbf{u}_t - \mathbf{M}\mathbf{p}\right) \end{pmatrix} \quad (20)$$

where the frame parameters $\mathbf{Q}$, $\mathbf{c}$ are with Eqs. (12)–(17) stored in $\mathbf{p}$:

$$\mathbf{p} = \begin{pmatrix} ap(\dot{\mathbf{S}}) \\ \dot{\mathbf{d}} \\ ap(\ddot{\mathbf{S}}) \\ \ddot{\mathbf{d}} \\ ap(\dddot{\mathbf{S}}) \\ \dddot{\mathbf{d}} \end{pmatrix} \qquad (21)$$

Matrix $\mathbf{M}$ only depends on the underlying air flow $\mathbf{u}$, Jacobian $\mathbf{J} = \nabla \mathbf{u}$, the inertial particle velocity $\mathbf{v}$, gravity $\mathbf{g}$ and response time r:

$$\begin{aligned} \mathbf{M} = \quad & \frac{1}{r} \left(-\mathbf{J}\mathbf{x}_p + \mathbf{u}_p, \, \mathbf{J}, \, \mathbf{x}_p, \, -\mathbf{I}, \, \mathbf{0}_p, \, \mathbf{0}_{n \times n} \right) \\ + \; & \left(\mathbf{g}_p, \, \mathbf{0}_{n \times n}, \, 2\mathbf{v}_p, \, \mathbf{0}_{n \times n}, \, \mathbf{x}_p, \, -\mathbf{I} \right) \end{aligned} \qquad (22)$$

Thus in this notation, matrix $\mathbf{M}$ and vector $\mathbf{p}$ linearly separate the flow properties from the reference frame parameters. Note that in 2D, $\mathbf{M}$ is a 2×9 matrix and $\mathbf{p}$ is a 9-vector, while in 3D $\mathbf{M}$ is a 3×18 matrix and $\mathbf{p}$ is an 18-vector. This can be seen by considering that the subscript p produces in 2D a vector and in 3D a matrix, cf. the definition in Eq. (1).

4.3 Finding the Optimal Frame

As discussed by Lugt [43] and Robinson [53], the optimal frame is the one in which the observed flow becomes steady. However, it is generally not possible to find a single *global* reference frame, in which the entire flow appears steady everywhere [43], since vortices might move at different locations in different directions. For this reason, we search at each point $(\mathbf{x},t)$ in the domain for a *local* reference frame $(\mathbf{Q},\mathbf{c})$ in which a neighborhood region U appears steady:

$$\int_U \| \tilde{\mathbf{u}}_t^* \|^2 \, dV \rightarrow \min \qquad (23)$$

Following Günther et al. [22], we assume that $\mathbf{Q}(t)$ and $\mathbf{c}(t)$ are spatially-constant in a small neighborhood U around $(\mathbf{x},t)$, which makes Eqs. (18)–(20) applicable. By waving the spatial and temporal connection of neighboring points, the search for optimal reference frames is local and easily parallelized. For this, we set $\mathbf{Q} = \mathbf{I}$, $\mathbf{c} = \mathbf{0}^1$ and locally solve for the derivatives $\dot{\mathbf{Q}}$, $\ddot{\mathbf{Q}}$, $\dot{\mathbf{c}}$ and $\ddot{\mathbf{c}}$. Due to the linearity of $\tilde{\mathbf{u}}_t^*$ in Eq. (20), the local reference frame in which the high-dimensional flow becomes steady is found by linearly solving:

$$\widehat{\mathbf{M}} \, \mathbf{p} = \widehat{\mathbf{y}} \qquad (24)$$

with system matrix $\widehat{\mathbf{M}}$ and right hand side $\widehat{\mathbf{y}}$

$$\begin{aligned} \widehat{\mathbf{M}} &= \int_U \mathbf{M}^{\mathrm{T}} \mathbf{M} \, dV \qquad &(25) \\ \widehat{\mathbf{y}} &= \frac{1}{r} \int_U \mathbf{M}^{\mathrm{T}} \mathbf{u}_t \, dV. \qquad &(26) \end{aligned}$$

After computing the optimal reference parameters in Eq. (21), we apply Eqs. (18)–(20) to obtain the high-dimensional vector field and its derivatives in the optimal frame. In Appendix A, we show that the Galilean invariant method of Günther and Theisel [25] is a special case.

4.4 Regularization

Unfortunately, Eq. (25) does not give a full-rank matrix $\widehat{\mathbf{M}}$. With Eq. (22), we can see that the rows of $\mathbf{M}^{\mathrm{T}}\mathbf{M}$ have linear dependencies, no matter where $\mathbf{M}^{\mathrm{T}}\mathbf{M}$ is sampled. In the following, we show this for the 3D case. The expressions are analogue for 2D. For brevity, we denote only in this section $\mathbf{0} = \mathbf{0}_{3 \times 3}$ as the zero matrix and use as usual $\mathbf{I}$ for the identity matrix. Since r is a constant, the first dependency is:

$$\mathbf{M}^{\mathrm{T}}\mathbf{M} \, (\mathbf{0}, \mathbf{0}, \mathbf{0}, r \cdot \mathbf{I}, \mathbf{0}, \mathbf{0})^{\mathrm{T}} = \mathbf{M}^{\mathrm{T}}\mathbf{M} \, (\mathbf{0}, \mathbf{0}, \mathbf{0}, \mathbf{0}, \mathbf{0}, \mathbf{I})^{\mathrm{T}} . \qquad (27)$$

---
[1] By setting $\mathbf{Q} = \mathbf{I}$ and $\mathbf{c} = \mathbf{0}$, we select the solution at $\mathbf{x}$. During the derivation, the symbols are still required to incorporate their derivatives correctly.

Further, if we sample neighborhood U in space only (i.e., $\mathbf{v}_p$ is constant for all samples), another dependency in $\mathbf{M}^{\mathrm{T}}\mathbf{M}$ has the form

$$\mathbf{M}^{\mathrm{T}}\mathbf{M} \, (\mathbf{0}, \mathbf{0}, \mathbf{0}, \mathbf{0}, \mathbf{I}, \mathbf{0})^{\mathrm{T}} - \mathbf{M}^{\mathrm{T}}\mathbf{M} \, (\mathbf{0}, \mathbf{0}, r \cdot \mathbf{I}, \mathbf{0}, \mathbf{0}, \mathbf{0})^{\mathrm{T}} \qquad (28)$$

$$= \mathbf{M}^{\mathrm{T}}\mathbf{M} \, (\mathbf{0}, \mathbf{0}, \mathbf{0}, \mathbf{0}, \mathbf{0}, 2r \cdot \mathbf{v}_p)^{\mathrm{T}}. \qquad (29)$$

We cope with this by regularization. Instead of Eq. (25), we use

$$\widehat{\mathbf{M}} = \int_U \mathbf{M}^{\mathrm{T}}\mathbf{M} \, dV + \mathbf{E} \qquad (30)$$

where $\mathbf{E}$ is a diagonal matrix with the last $3n - 3$ entries being set to 1. The regularization in Eq. (30) enforces that the last $3n - 3$ components of the optimal $\mathbf{p}$ are zero.

4.5 Dependence on Particle Velocity

We now study how the solution of Eqs. (24), (26) and (30) depends on the particle velocity $\mathbf{v}$. The optimal reference frame parameters in $\mathbf{p}$ have the following properties: $ap(\dot{\mathbf{S}})$, $\dot{\mathbf{d}}$, $ap(\ddot{\mathbf{S}})$, $ap(\dddot{\mathbf{S}})$ and $\dddot{\mathbf{d}}$ do not depend on $\mathbf{v}$. In fact, the regularization in Eq. (30) gives $ap(\dddot{\mathbf{S}}) = 0$ and $\dddot{\mathbf{d}} = \mathbf{0}$. Only $\ddot{\mathbf{d}}$ depends linearly on $\mathbf{v}_p$, which follows from Eq. (22). To see this, consider the Maple sheet in the additional material. Next, we discuss how $\mathbf{v}$ is chosen to compute the correct parameter $\ddot{\mathbf{d}}$. For this, we look at the vortex core in both 2D and 3D, since the vortex criterion gives us another condition to pin down the linear dependence.

2D Case. To find vortices in 2D, we search for locations where $\tilde{\mathbf{u}}^*$ in Eq. (18) vanishes in the optimal frame. The vanishing spatial subspace in $\tilde{\mathbf{u}}^* = \mathbf{0}$ gives for our local $\mathbf{Q} = \mathbf{I}$:

$$\mathbf{v} = -\dot{\mathbf{S}} \, \mathbf{x} - \dot{\mathbf{d}} . \qquad (31)$$

Since $\dot{\mathbf{S}}$ and $\dot{\mathbf{d}}$ are the same for all $\mathbf{v}$, we can solve Eqs. (24), (26) and (30) for an arbitrary $\mathbf{v}$ to obtain $\dot{\mathbf{S}}$, $\ddot{\mathbf{S}}$ and $\dot{\mathbf{d}}$ from Eq. (21). Without loss of generality, we set $\mathbf{v} = \mathbf{0}$ and insert the resulting $\dot{\mathbf{S}}$ and $\dot{\mathbf{d}}$ into Eq. (31) to obtain the particle velocity $\mathbf{v}$, for which $\tilde{\mathbf{u}}^*$ in Eq. (18) vanishes. After computing $\ddot{\mathbf{d}}$ by solving Eqs. (24), (26) and (30) again with Eq. (31), we insert Eq. (31) into the velocity subspace of Eq. (18). With the critical point condition $\tilde{\mathbf{u}}^* = \mathbf{0}$, we arrive at a local criterion that can be conveniently searched in the spatial domain:

$$\frac{\mathbf{u}(\mathbf{x},t) - \mathbf{v}}{r} + \mathbf{g} + 2\dot{\mathbf{S}}\mathbf{v} + (\ddot{\mathbf{S}} + \dot{\mathbf{S}}\dot{\mathbf{S}})\mathbf{x} + \ddot{\mathbf{d}} + \dot{\mathbf{S}}\dot{\mathbf{d}} = \mathbf{0} , \qquad (32)$$

which gives the vortex centers of inertial particles in the 2D case.

3D Case. In 3D, we similarly determine the dependence of $\ddot{\mathbf{d}}$ on $\mathbf{v}$. Instead of solving for $\mathbf{v}$ directly, we insert the linear dependence into the vortex criterion. First, $\ddot{\mathbf{d}}$ depends on $\mathbf{v}$ as follows:

$$\ddot{\mathbf{d}} = \ddot{\mathbf{d}}_0 - ap(\mathbf{q}) \, \mathbf{v}. \qquad (33)$$

In order to obtain $\ddot{\mathbf{d}}_0$ and $\mathbf{q}$, we solve Eqs. (24), (26) and (30) twice with two different $\mathbf{v}$.

In 3D, we search for the locations $(\mathbf{x}, \mathbf{v})$ with $\tilde{\mathbf{J}}^* \, \tilde{\mathbf{u}}^* \parallel \tilde{\mathbf{u}}^*$, which is the direct extension of Sujudi-Haimes [69], which was shown to work well for massless particles in their optimal frame [22]. The condition $\tilde{\mathbf{J}}^* \, \tilde{\mathbf{u}}^* \parallel \tilde{\mathbf{u}}^*$ is a parallel vectors operation in 6D. By locally setting $\mathbf{Q} = \mathbf{I}$, Eq. (18) and Eq. (19) give

$$\tilde{\mathbf{u}}^* = \begin{pmatrix} \mathbf{v} + \mathbf{a} \\ \mathbf{B}\mathbf{v} + \mathbf{b} \end{pmatrix} , \quad \tilde{\mathbf{J}}^* \, \tilde{\mathbf{u}}^* = \tilde{\mathbf{w}}^* = \begin{pmatrix} \mathbf{B}\mathbf{v} + \mathbf{b} \\ \mathbf{C}\mathbf{v} + \mathbf{c} \end{pmatrix} \qquad (34)$$
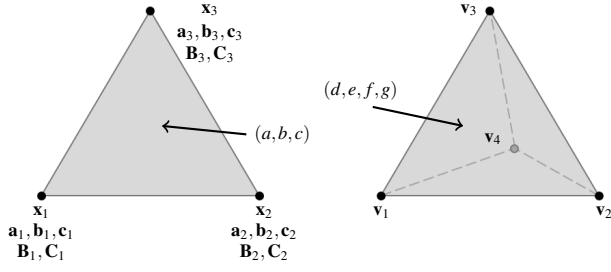
Fig. 1: Setup for the barycentric interpolation: Given the vectors $\mathbf{a}_i$, $\mathbf{b}_i$, $\mathbf{c}_i$ and the matrices $\mathbf{B}_i$ and $\mathbf{C}_i$ on a triangle, and four velocities $\mathbf{v}_i$ on a tetrahedron, the 6D vectors $\tilde{\mathbf{u}}^*$ and $\tilde{\mathbf{w}}^*$ can be linearly interpolated.

Fig. 2: Recursive root finding principle by Bezier subdivision in 2D. If all control points are positive (or all are negative), the Bezier curve cannot intersect the x-axis, since the curve is always inside the convex hull of the control points (left). If there are control points above and below the x-axis, the curve might intersect (center and right).

where Eq. (33) is inserted, giving

$$\mathbf{a} = \dot{\mathbf{S}}\mathbf{x} + \dot{\mathbf{d}} \tag{35}$$

$$\mathbf{B} = 2\dot{\mathbf{S}} - \frac{1}{r}\mathbf{I} - a p(\mathbf{q}) \tag{36}$$

$$\mathbf{b} = \frac{\mathbf{u}}{r} + \mathbf{g} + (\ddot{\mathbf{S}} + \dot{\mathbf{S}}\dot{\mathbf{S}})\mathbf{x} + \ddot{\mathbf{d}}_0 + \dot{\mathbf{S}}\dot{\mathbf{d}} \tag{37}$$

$$\mathbf{H}_1 = \frac{1}{r}\mathbf{J} + \frac{1}{r}\dot{\mathbf{S}} - \dot{\mathbf{S}}\dot{\mathbf{S}} + \ddot{\mathbf{S}} \tag{38}$$

$$\mathbf{H}_2 = -\frac{1}{r}\mathbf{I} + 2\dot{\mathbf{S}} \tag{39}$$

$$\mathbf{C} = \mathbf{H}_1 + \mathbf{H}_2 \, \mathbf{B} \tag{40}$$

$$\mathbf{c} = \mathbf{H}_1 \, \mathbf{a} + \mathbf{H}_2 \, \mathbf{b} \, . \tag{41}$$

Note that all quantities from Eq. (35)–(41) are independent of $\mathbf{v}$ and can thus be discretized in the spatial domain. We search for the locations $(\mathbf{x}, \mathbf{v})$ where the two 6D vector fields $\tilde{\mathbf{u}}^*$ and $\tilde{\mathbf{w}}^*$, defined in Eq. (34), are parallel. Next, we describe the 6D parallel vectors extraction.

4.6 Parallel Vectors in 6D

Aside from the usual 3D parallel vectors (PV) extractors [49, 78], a 5D parallel vectors operator of Oster et al. [48] exists in the context of eigenvector analysis. We are not aware of any existing 6D parallel vectors approach. In the following, we derive an extraction algorithm that is tailored to our two 6D vector fields in Eq. (34).

Since all elements in Eqs. (35)–(41) are independent of $\mathbf{v}$, we can discretize them onto a piecewise linear tetrahedral grid and interpolate them only in the spatial domain. Thus, at three spatial grid points $\mathbf{x}_i$ with $i \in \{1, 2, 3\}$, we have computed $\mathbf{a}_i, \mathbf{b}_i, \mathbf{c}_i, \mathbf{B}_i, \mathbf{C}_i$. Inside the triangle, we assume a linear interpolation with the barycentric coordinates a, b, c:

$$\mathbf{a} = a\,\mathbf{a}_1 + b\,\mathbf{a}_2 + c\,\mathbf{a}_3 \tag{42}$$

$$\mathbf{b} = a\,\mathbf{b}_1 + b\,\mathbf{b}_2 + c\,\mathbf{b}_3 \tag{43}$$

$$\mathbf{c} = a\,\mathbf{c}_1 + b\,\mathbf{c}_2 + c\,\mathbf{c}_3 \tag{44}$$

$$\mathbf{B} = a\,\mathbf{B}_1 + b\,\mathbf{B}_2 + c\,\mathbf{B}_3 \tag{45}$$

$$\mathbf{C} = a\,\mathbf{C}_1 + b\,\mathbf{C}_2 + c\,\mathbf{C}_3 \tag{46}$$

with $a + b + c = 1$. Further, we consider $\mathbf{v}$ to be linearly interpolated between 4 vectors $\mathbf{v}_1, \mathbf{v}_2, \mathbf{v}_3, \mathbf{v}_4$:

$$\mathbf{v} = d\,\mathbf{v}_1 + e\,\mathbf{v}_2 + f\,\mathbf{v}_3 + g\,\mathbf{v}_4 \tag{47}$$

with $d + e + f + g = 1$. Fig. 1 illustrates the setup. Inserting Eqs. (42)–(47) into Eq. (34) gives $\tilde{\mathbf{u}}^*$ and $\tilde{\mathbf{w}}^*$ in barycentric coordinates $(a, \ldots, g)$. To search for locations of parallelity, we consider the 6×6 matrix $\tilde{\mathbf{X}}$ defined by

$$\tilde{\mathbf{X}}_{i,j} = \tilde{\mathbf{u}}_i^* \, \tilde{\mathbf{w}}_j^* - \tilde{\mathbf{w}}_i^* \, \tilde{\mathbf{u}}_j^* \tag{48}$$

for the element indices $i, j \in \{1, \ldots, 6\}$. Note that $\tilde{\mathbf{X}}$ is a skew symmetric matrix with vanishing diagonal that can be interpreted as 6D generalization of the 3D cross product. With Eq. (48), we have:

$$\tilde{\mathbf{u}}^* \parallel \tilde{\mathbf{w}}^* \iff \tilde{\mathbf{X}} = \mathbf{0}_{6 \times 6} \, . \tag{49}$$

Thus, the search for parallel vectors becomes a search for roots in all entries of matrix $\tilde{\mathbf{X}}$. Since $\tilde{\mathbf{X}}$ is skew-symmetric, only the upper (or lower) triangular matrix needs to be tested. Matrix $\tilde{\mathbf{X}}$ is a quadratic function in the barycentric coordinates $(a, \ldots, g)$. We use a Bezier-based subdivision to find the roots [36, 54]. Thus, we represent the matrix in Bernstein-Bezier form, as:

$$\tilde{\mathbf{X}}(a,b,c;d,e,f,g) = \sum_{i+j+k=2} \sum_{l+m+n+o=2} B^2_{i,j,k} \, B^2_{l,m,n,o} \, \tilde{\mathbf{B}}_{i,j,k;l,m,n,o} \tag{50}$$

where $\tilde{\mathbf{B}}_{i,j,k;l,m,n,o}$ are 60 Bezier matrices (in generalization of the usual concept of Bezier points) and

$$B^2_{i,j,k} = \frac{2!}{i! \, j! \, k!} \, a^i \, b^j \, c^k \;, \quad B^2_{l,m,n,o} = \frac{2!}{l! \, m! \, n! \, o!} \, d^l \, e^m \, f^n \, g^o \tag{51}$$

are the Bernstein polynomials of degree 2. We obtains the unknown Bezier matrices by sampling $\tilde{\mathbf{X}}$ at 60 points:

$$\tilde{\mathbf{X}}_{i,j,k;l,m,n,o} = \tilde{\mathbf{X}}\left(\frac{i}{2}, \frac{j}{2}, \frac{k}{2}; \frac{l}{2}, \frac{m}{2}, \frac{n}{2}, \frac{o}{2}\right) \tag{52}$$

for all $i, j, k, l, m, n, o \in \{0, 1, 2\}$ with $i + j + k = l + m + n + o = 2$. The points are placed on the vertices and edge mid-points of the spatial triangle and the velocity tetrahedron, respectively. Then, the Bezier matrices are obtained by

$$\tilde{\mathbf{B}}_{2,0,0;2,0,0,0} = \tilde{\mathbf{X}}_{2,0,0;2,0,0,0} \tag{53}$$

$$\tilde{\mathbf{B}}_{1,1,0;2,0,0,0} = 2\,\tilde{\mathbf{X}}_{1,1,0;2,0,0,0} - \frac{\tilde{\mathbf{X}}_{2,0,0;2,0,0,0} + \tilde{\mathbf{X}}_{0,2,0;2,0,0,0}}{2}$$

$$\tilde{\mathbf{B}}_{2,0,0;1,1,0,0} = 2\,\tilde{\mathbf{X}}_{2,0,0;1,1,0,0} - \frac{\tilde{\mathbf{X}}_{2,0,0;2,0,0,0} + \tilde{\mathbf{X}}_{2,0,0;0,2,0,0}}{2}$$

$$\tilde{\mathbf{B}}_{1,1,0;1,1,0,0} = 4\,\tilde{\mathbf{X}}_{1,1,0;1,1,0,0} - \tilde{\mathbf{X}}_{2,0,0;1,1,0,0} - \tilde{\mathbf{X}}_{0,2,0;1,1,0,0}$$
$$- \tilde{\mathbf{X}}_{1,1,0;2,0,0,0} - \tilde{\mathbf{X}}_{1,1,0;0,2,0,0}$$
$$+ \frac{1}{4}(\tilde{\mathbf{X}}_{2,0,0;2,0,0,0} + \tilde{\mathbf{X}}_{0,2,0;2,0,0,0}$$
$$+ \tilde{\mathbf{X}}_{2,0,0;0,2,0,0} + \tilde{\mathbf{X}}_{0,2,0;0,2,0,0}) \, . \tag{54}$$

The remaining Bezier matrices follow by symmetry considerations. Then, a subdivision-based search for parallel vectors locations is based on the following observation: if an entry (i, j) of all 60 Bezier matrices is positive (or if all 60 entries are negative), then – due to the convex hull property of Bernstein-Bezier representations – $\tilde{\mathbf{X}}$ cannot vanish for barycentric coordinates between 0 and 1. Contrary, if all entries have both positive and negative values in the 60 Bezier matrices, no statement about the existence of parallel vectors locations is possible, see Fig. 2 for a 2D illustration. In this case, a recursive subdivision of the spatial triangle or the $\mathbf{v}$ tetrahedron is done. For this, we alternate between a subdivision in the spatial domain and the velocity domain.

5 IMPLEMENTATION

We implemented the reference frame extraction, the 2D critical point search and the 6D parallel vectors extraction in C++ with dynamically scheduled multi-threading using OpenMP.

Numerical Optimization. The reference frame extraction is based on the open source implementation for the massless case by Günther et al. [22]. The least squares problem in Eq. (24) is numerically solved using a Householder QR decomposition with full-pivoting, using the linear algebra library Eigen. The critical point search for the 2D case follows the common recursive subdivision algorithm of Globus et al. [19].

Recursive Subdivision in 6D PV. The numerical data sets were initially given on regular grids and the analytical flows were sampled onto regular grids. The resolutions are later given in Table 1. For the 6D parallel vectors extraction, we first tetrahedralize the given data sets. Since we search for line structures, we compute PV points on the triangle faces of the spatial tetrahedra mesh and connect the PV points on the faces with line segments. In the spatial domain, triangles are split into four equally-sized triangles, as illustrated by Oster et al. [48]. In the velocity domain, we search inside the tetrahedra for the velocity that corresponds to the PV solution. For the recursive subdivision of a tetrahedron in the velocity domain, we follow the subdivision scheme of Schaefer et al. [62], which results in four tetrahedra and an octahedron in the middle. The latter is further subdivided into four tetrahedra. In all examples, we terminated the subdivision after 30 recursive steps.

6 RESULTS

Next, we apply the above inertial vortex coreline extraction algorithms in 2D and 3D vector fields. In all example, we set as particle density $\rho_p = 2650\,kg/m^3$, which corresponds to Quartz glass. The particle diameter d_p varies in the range from $90\,\mu m$ to $150\,\mu m$. As viscosity we set $\mu = 1.532 \times 10^{-5}\,kg/(m \cdot s)$, which equates to air. If not mentioned otherwise, the gravity vector is set to $\mathbf{g} = (0,1,0)^T$.

6.1 Elliptic Beads

Our first synthetic test case contains an analytic unsteady 2D vector field, in which two vortices rotate around each other. The vector field is defined as the co-gradient of a stream function $s(x,y,t)$:

$$\mathbf{v}^* = \begin{pmatrix} -\frac{\partial s}{\partial y} \\ \frac{\partial s}{\partial x} \end{pmatrix} \quad \text{with} \quad s(x,y,t) = (a+b)(1-a-b)\,, \quad (55)$$

$a(x,y,t) = \frac{(3x\cos(t)+3y\sin(t)-1)^2}{36}$ and $b(x,y,t) = (x\sin(t) - y\cos(t))^2$. In this flow, the vortices move on circular paths, and thus Galilean invariance does not apply. Fig. 3 shows the vortex corelines that were extracted with the Galilean invariant approach of Günther and Theisel [25] and our new objective method using a neighborhood size of $U = 11^2$. To test the quality of the vortex corelines, we release inertial particles with diameter $d_p = 90\,\mu m$ in the vicinity of the corelines and observe whether they stay close to the coreline and rotate around it. Our objective method passes this test, while the Galilean invariant method returns several incorrect answers.

6.2 2D Cylinder

Next, we compare our objective method with the Galilean invariant approach in a numerically simulated flow, in which the vortices move with almost constant speed in a constant direction. In this case, Galilean invariance is a valid assumption and the results are hypothesized to be similar. Using Gerris flow solver [52], we simulated a von-Kármán vortex street with Reynolds number 160 in a channel with no-slip boundary. Fig. 4 displays the vortex cores that were extracted for inertial particles with diameter $d_p = 100\,\mu m$, and with a neighborhood size of $U = 21^2$. Due to the inherent smoothing in Eq. (30) by neighborhood U, the objective method is less sensitive to noise. The overall vortex locations are identical as expected. The LIC visualizations in the background show the vector fields, in which the critical points were searched, i.e., Eq. (59) (Galilean invariant) and Eq. (32) (our objective method). The LIC visualization of the Galilean invariant approach is more noisy, as this approach is completely local, whereas our approach is more robust due to the fitting of the reference frame to a small neighborhood.

(a) Galilean invariant vortex corelines   (b) Objective vortex corelines
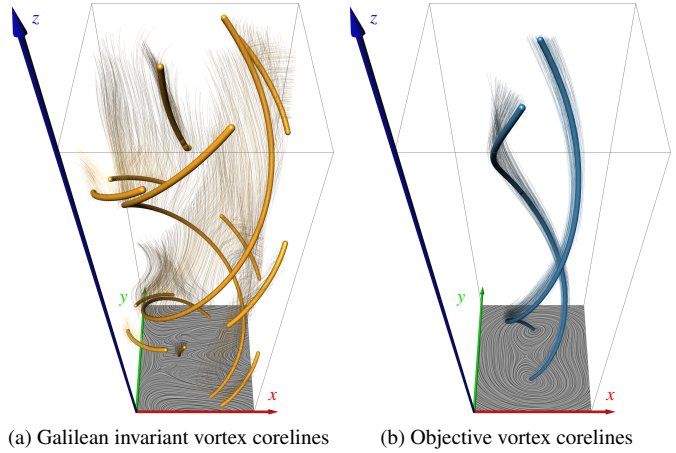
Fig. 3: Space-time visualizations in the ELLIPTIC BEADS. If vortices move on rotating paths, Galilean invariance is insufficient. Inertial pathlines stay near the objective coreline, indicating a rotating motion.
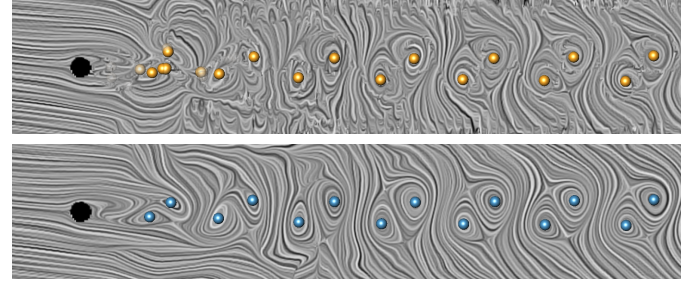
Fig. 4: Vortex cores in the 2D CYLINDER flow. Top: Galilean invariant method and bottom: our objective technique. Due to the inherent smoothing within neighborhood U, the objective technique is less senstive to noise. The swirling strength [81] is mapped to transparency, showing that near the end of the domain vortices become weaker. The LIC visualization shows the fields $\mathbf{u} - \mathbf{f} + r\mathbf{g}$ (top) and Eq. (32) (bottom).

6.3 Boussinesq

Our next example contains a more turbulent scenario. Using Gerris flow solver [52], we performed a convection simulation around a heated cylinder. In the wake of the cylinder, a fast jet stream induces vortical motion. As shown in Fig. 5, the Galilean invariant method produces numerous false positives, while the objective method finds less but more stable vortices, which is apparent in the supplemental video. Since LIC does not encode the vector magnitude, differences are seen at the beginning of the video in areas, where the flow is standing almost still. The vortex cores were extracted for inertial particles with diameter $d_p = 100\,\mu m$, and we used a neighborhood size of $U = 11^2$. The transparency of the extracted vortex cores corresponds to the swirling strength, which is a measure for the strength of the rotating motion.

6.4 Chimera

Our last 2D case was numerically simulated using the cut-cell method of Azevedo et al. [2]. This simulation contains an oscillating rod that stirs a fluid flow in a 2D domain into motion. The rod itself interacts with the vortices, creating more complex motions for which Galilean invariance is not always an adequate assumption. As shown in Fig. 6 for $d_p = 100\,\mu m$, the vortex locations differ in the fast moving areas of the domain, which occur close to the obstacle. In addition, our objective method contains less noise. As neighborhood size we selected $U = 21^2$. Other choices are discussed later in Section 6.8.1. As in the example above, the swirling strength is mapped to transparency, which emphasizes the clear and strong vortices.
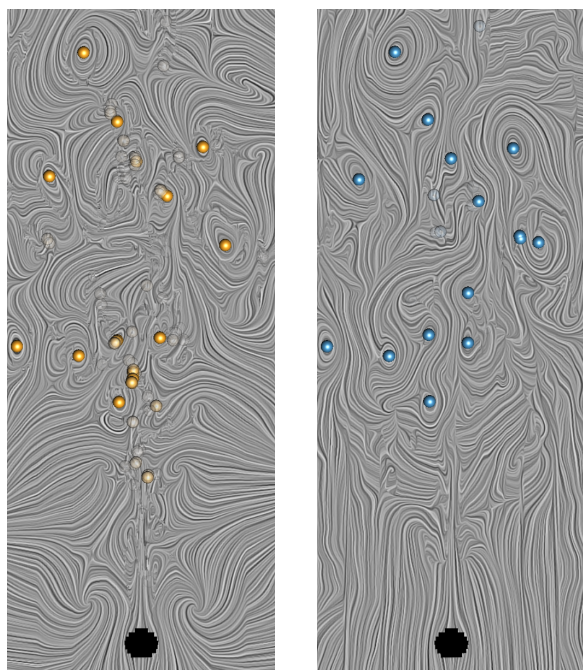
(a) Galilean inv. vortex corelines (b) Objective vortex corelines

Fig. 5: Galilean invariant and objective vortex cores in the BOUSSI-NESQ flow. Aside from the sensitivity to noise, differences can be seen close to the jet core, in which vortices move with higher speed. Here, for $d_p = 100\,\mu m$ and with a neighborhood size of $U = 11^2$.

6.5 Rotating 3D Center

Next, we utilize an analytic time-dependent 3D flow, described by Günther et al. [24], which contains a single vortex coreline, rotating around the z-axis.

$$\mathbf{v}(x,y,z,t) = \frac{1}{\sqrt{3}} \begin{pmatrix} (\cos(t) + \sin(t))z - y - \cos(t) + \frac{x^3}{1000} \\ (\cos(t) - \sin(t))z + x + \sin(t) + \frac{y^3}{1000} \\ (\sin(t) - \cos(t))y - (\sin(t) + \cos(t))x + 2 + \frac{z^3}{1000} \end{pmatrix}$$

(56)

In this example, Galilean invariance is not a valid assumption, since vortices do not move in a constant direction. Thus, we can expect different results for Galilean invariance and objectivity. Fig. 7 displays the corelines, extracted in this vector field using the Galilean invariant method and using our objective method with $U = 9^3$. For the small particle size of $d_p = 150\,\mu m$, our objective inertial coreline approaches the vortex coreline of the massless case. For the Galilean invariant approach this is not the case. Thus, in this flow, objectivity is a necessary requirement to successfully extract the vortex coreline.

6.6 Square Cylinder

Next, we compute the vortex corelines in a numerically simulated 3D SQUARE CYLINDER flow. In this vector field, vortices move with almost constant speed in a fairly constant direction. Thus, Galilean invariance is generally assumed to be a valid assumption [22, 25, 79]. Existing coreline extraction methods are *local*, which means they determine vortex corelines only based on the velocity and the derivatives at a given location. This locality allows for efficient implementations, but it is also strongly influenced by noise and discretization artifacts of the data. Fig. 8 shows the *unfiltered* inertial vortex corelines obtained with the local method from previous work [25] (left) and our method (right). In this example, gravity was set to $\mathbf{g} = (0,2,0)^{\mathsf{T}}$ and the diameter was $d_p = 100\,\mu m$. The local method results in many spurious and short vortex corelines, which may be filtered by line length. A
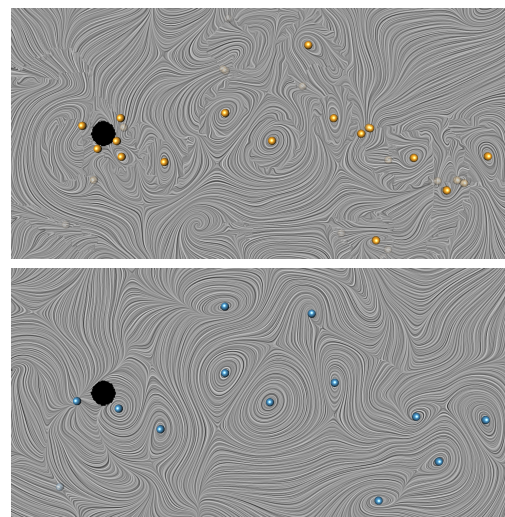
Fig. 6: Comparison of Galilean invariant [25] (top) and objective vortex cores (bottom) in the CHIMERA flow for a particle size of $d_p = 100\,\mu m$ and a neighborhood size of $U = 21^2$ voxels. Differences between the extraction results can be seen especially around the obstacle, since there the fluid is moving the fastest. See the video for an animation.
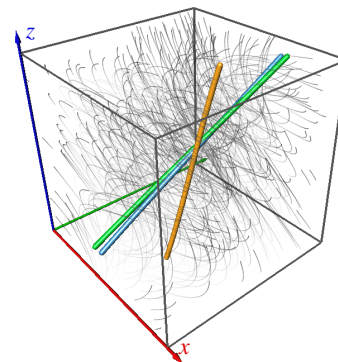
Fig. 7: Vortex corelines in the ROTATING 3D CENTER flow, including the massless case (green), Galilean invariance (orange) and our objective method (blue), here for $d_p = 150\,\mu m$. For such small particle sizes, our inertial corelines approach the coreline of the massless case, whereas the Galilean invariant case is far off. Streamlines of tracer particles are shown in gray as reference. See the video for an animation.

clean extraction typically requires post processing. Since our method inherently includes a smoothing within a small neighborhood U, the resulting extraction becomes much more robust. In fact, Fig. 8 shows the extraction results without any post-processing. Here, we used $U = 13^3$. This clean extraction result, however, is bought at the expense of a rather high computation time, since the extraction with our method took approximately 24 hours. The performance is discussed later in Section 6.9 in more detail. It should be noted, however, that our method is generally able to find vortices moving on arbitrarily rotating and translating paths, whereas previous work [25] only worked for the smaller class of equal-speed translations.

6.7 Buoyancy

Next, we extract inertial vortex corelines in a more turbulent BUOY-ANCY flow. In this flow, a plume is rising at the center of the domain. Fig. 9 shows that the plume creates a vortex ring at the ground and a vortex rope that is lofted into the air. Here, we extracted the inertial vortex corelines using the Galilean invariant approach [25] and our objective method for $\mathbf{g} = (0,2,0)^{\mathsf{T}}$, $d_p = 200\,\mu m$ and $U = 21^3$. The swirling strength [81] is mapped to the line radius. Again, the inherent smoothing of our objective method produces less noisy results than

Galilean invariant approach [25]   Our objective method
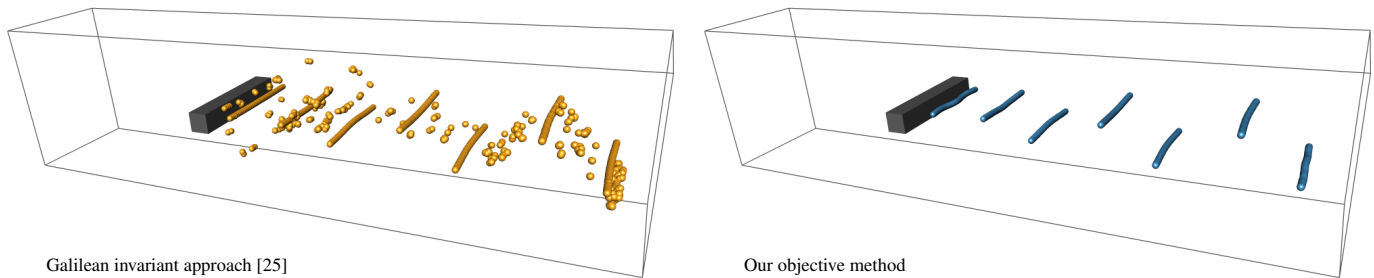
Fig. 8: We propose an energy minimization to determine the rotating and translating reference frame, in which the high-dimensional flow that governs finite-sized particle motion becomes as steady as possible. In this frame, we apply a Bezier-based recursive subdivision to extract the vortex corelines, which are defined by parallel vectors in 6D. Compared to the Galilean invariant approach of Günther and Theisel [25], our new objective method is far more robust and produces clean corelines. The visualizations above show the unfiltered corelines, i.e., the result directly produced by the parallel vectors extractor in the SQUARE CYLINDER flow.

(a) Galilean invariant approach [25]   (b) Our objective method
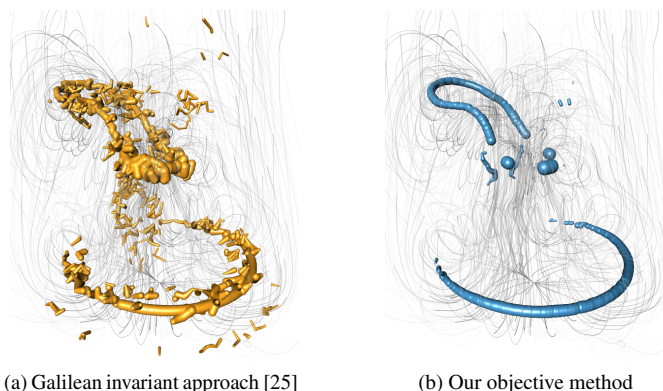
Fig. 9: In the BUOYANCY flow, a plume rises in the center of the domain, creating a vortex ring on the ground and a vortex rope that is carried upwards. The Galilean invariant approach [25] produces more noisy results compared to our objective method. Here, $d_p = 200\,\mu m$.

the Galilean invariant approach. Typically, the vortex coreline cleanup involves a heuristic connection of close line segments and a subsequent filtering by length. If the heuristics fail, errors occur, which is more likely if noisy line segments are present as in the Galilean invariant case. Again our improvement is bought with a longer computation time of 11 hours, as reported later in Section 6.9.

6.8 Parameters

6.8.1 Neighborhood U

The neighborhood size U determines the region around a given point to which the local optimal reference frame transformation is fitted. We inherit this parameter from Günther et al. [22], who discussed it already with examples. In summary, the smaller the region, the more sensitive is the optimization to noise and velocity discretization artifacts. Thus, increasing the neighborhood size U, makes the method more robust. The larger the region, however, the greater the risk to have multiple vortices inside the region, traveling into different directions. In this case, one estimated reference transformation cannot fit to all vortex movements. Thus, in principle, the neighborhood size should be small enough to contain only a single vortex, yet be large enough to be robust. In practice, we compute the optimal reference frame for a range of different neighborhoods and manually inspect the resulting flow in the optimal reference frame, as shown in Fig. 10. In this example, the smallest neighborhood size of $U = 11^2$ voxels already contains the dominant vortex structures, but is still noisy. Increasing the size to $U = 21^2$ makes the vortices more apparent and increasing the size even further to $U = 31^2$ does not significantly change the main vortex locations. Thus, in this case, a value of $U = 21^2$ seems appropriate.

6.8.2 Mass Dependence

As demonstrated by Günther and Theisel [25], the location of inertial vortex corelines depends on the particle response time r and the gravity **g**. The particle sizes that are studied depend on the application. For instance, in controlled experimental setups, a finite set of different particle sizes may be used [7]. In the modeling of real-world scenarios, heterogeneous mixtures might be studied instead, such as in helicopter brownout engineering [70, 71]. In the latter case, a finite number of inertial particles sizes might be uniformly sampled from the range of possible particle sizes, such that occlusion is tolerable and the continuous mass spectrum is represented.

6.8.3 Velocity Subspace

In the 3D case, we apply a full 6D parallel vectors search in both the spatial and the velocity domain. The spatial domain is given by the underlying data set. For the velocity domain, however, the bounding box of all realizable particle velocities is required. The underlying slowly attracting manifold provides the velocity that inertial particles approach in the limit [34], from which the maximal velocity magnitude can be inferred. However, this is only an approximate solution, as it considers the limit case. Further, the initial velocity $\mathbf{v}_0$ needs to be considered as potential maximum, in case inertial particles are released with even higher velocity. In practice, we conservatively increase the velocity bounding box obtained from the initial velocity and the attracting manifold, sampled at the spatial grid coordinates, by 50%, which worked well for us in all examples.

6.9 Performance

We compare the timings of the former Galilean invariant method by Günther and Theisel [25] with our new objective method in Table 1. All measurements were taken on an Intel Core i7-6700K CPU with 4.0 GHz and 32 GB RAM. We separate between the computation of the optimal reference frame and the extraction of the vortex corelines. In case of the Galilean invariant method, we list the timings required to compute the derived vector field from which the vortices are extracted afterwards. The computation of the optimal frame is with our general method more expensive, as it involves the optimization of the reference frame. The extraction time in 2D strongly depends on the number of false-positives. In the Galilean invariant case, many small line segments are found in the simple data sets, which slows down the extraction time significantly. In the more complicated numerical flows, the extraction time is nearly identical, since both methods ultimately rely on a critical point search. The 3D extraction, however, is with our method far more expensive, since a full 6D parallel vectors search is required, while the search simplifies for Galilean invariance to a 3D PV problem.

6.10 Discussion

6.10.1 Unique Solution for Optimal Reference Frame

We inherit the uniqueness of the solution from the optimization approach for massless flows by Günther et al. [22]. The linear system

8

| (a) Neighborhood size $U = 11^2$ voxels. | (b) Neighborhood size $U = 21^2$ voxels. | (c) Neighborhood size $U = 31^2$ voxels. |
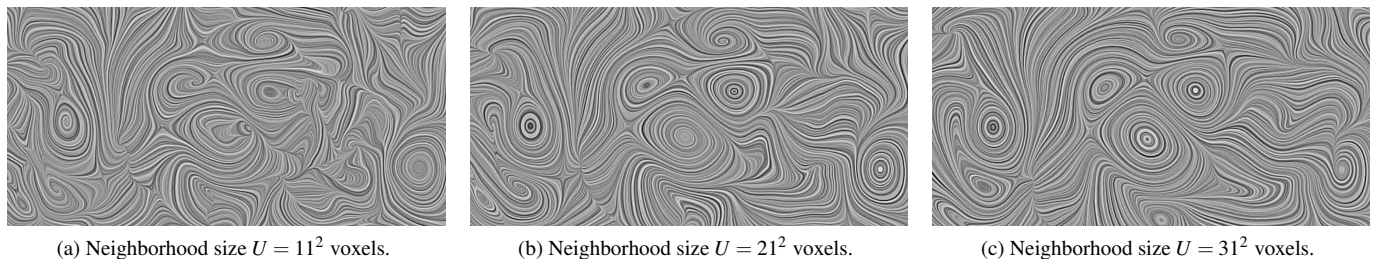
Fig. 10: Comparison of different neighborhood sizes in the CHIMERA flow. Here, the flow is shown in the optimal reference frame. The dominant structures are already present at small neighborhoods (left). By increasing the neighborhood size (middle and right), the vortices become clearer.

	Data set	Figure	Optimal frame Galilean	Optimal frame Objective	Vortex extraction Galilean	Vortex extraction Objective	Grid Resolution
2D	ELLIPTIC BEADS	Fig. 3	0.97 sec	40.47 sec	172.4 sec	0.99 sec	$128 \times 128 \times 256$
	2D CYLINDER	Fig. 4	19.68 sec	274.6 sec	607.8 sec	15.38 sec	$640 \times 80 \times 1501$
	BOUSSINESQ	Fig. 5	21.59 sec	300.4 sec	433.1 sec	440.0 sec	$600 \times 200 \times 667$
	CHIMERA	Fig. 6	4.20 sec	153.2 sec	138.7 sec	163.7 sec	$127 \times 63 \times 2000$
3D	ROTATING 3D CENTER	Fig. 7	0.23 sec	1.83 min	0.26 sec	4.6 hrs	$64 \times 64 \times 64$
	SQUARE CYLINDER	Fig. 8	0.65 sec	3.78 min	1.92 sec	20.75 hrs	$192 \times 64 \times 48$
	BUOYANCY	Fig. 9	0.35 sec	1.42 min	0.21 sec	11.9 hrs	$47 \times 95 \times 47$

Table 1: Computation time of the optimal frame and extraction time of vortex corelines, using the former Galilean invariant approach [25] and our more general optimal reference frame selection. In 2D, we list the extraction time for the entire space-time domain and in 3D, the extraction time for a single time step is reported. The computation of the optimal reference frame is linear in the grid resolution and the extraction of the vortex corelines is output-sensitive, i.e., the runtime scales with the number of features.

in Eq. (24) always has a unique solution, unless the underlying vector field $\mathbf{u}(\mathbf{x}, t)$ is either linear or rotationally-symmetric. The linear case is irrelevant on numerical data and the perfect rotational symmetry is structurally unstable and unlikely to occur in practice. In the analytical case in Eq. (56), we added a small cubic term to each component in order to make the system solvable.

6.10.2 Duplicate Roots in Bezier Subdivision

Similar to subdivision-based approaches for critical point search [19], roots will numerically appear multiple times, which requires a removal of duplicate solutions. Thus, we maintain a list of already found solutions and reject roots if they are too close to previously found ones.

6.10.3 Practical Concerns

As shown in Section 6.9, the generality and flexibility to adapt to any smooth rotation and translation of the reference frame, increases the computation time especially in 3D by orders of magnitude. This step, however, is necessary in case vortices are performing more complex movements than mere equal-speed translations. With our approach, users can favor quality (and correctness) over speed. For a wider adaption in practical workflows, we would like to study other 6D PV extraction approaches in the future, since this is currently the bottleneck. For instance, particle-based feature extractors have recently been discussed by Kindlmann et al. [41], which could be extended to 6D.

7 CONCLUSIONS

In this paper, we presented the first objective vortex coreline extractor for the tracking of inertial particles, i.e., particles with a finite mass. The method is based on the observation that features in time-dependent flows are best extracted in reference frames, in which the flow appears steady [22, 43, 53]. Starting from the derivation of the reference frame transformation, we observed that the temporal derivative can be minimized via a linear optimization. The dependence on the particle velocity can be resolved, when considering the vortex criteria in the optimal frame, which ultimately leads to a 2D critical point search for underlying 2D flows and a 6D parallel vectors operation for underlying 3D flows. By using the 6D PV fields, we described a Bezier-based subdivision algorithm that extracts the inertial vortex corelines of 3D

flows. At the moment, the 6D parallel vectors operation is quite expensive, which is why we would like to investigate faster extraction approaches in the future. Despite the higher computation time, the extraction quality is superior compared to the Galilean invariant method and the technique is generally more flexible and able to extract vortices of inertial particles moving on any smooth rotating or translating path.

A GALILEAN INVARIANCE

Studying special cases with known solution gives evidence for the correctness of a generalized method. In the following, we analyze our solution for Galilean transformations, for which inertial vortex corelines were studied by Günther and Theisel [25]. For the Galilean invariance case, we have $\mathbf{Q} = \mathbf{I}$, $\dot{\mathbf{S}} = \ddot{\mathbf{S}} = \dddot{\mathbf{S}} = \mathbf{0}_{n \times n}$ and $\ddot{\mathbf{d}} = \dddot{\mathbf{d}} = \mathbf{0}$. This gives for Eq. (18) and Eq. (20):

$$\tilde{\mathbf{u}}^* = \begin{pmatrix} \mathbf{v} + \dot{\mathbf{d}} \\ \frac{\mathbf{u} - \mathbf{v}}{r} + \mathbf{g} \end{pmatrix} \tag{57}$$

$$\tilde{\mathbf{u}}_t^* = \begin{pmatrix} \mathbf{0} \\ \frac{1}{r}(\mathbf{u}_t - \mathbf{J}\dot{\mathbf{d}}) \end{pmatrix} \tag{58}$$

Setting $\tilde{\mathbf{u}}_t^* = \mathbf{0}$ gives $\dot{\mathbf{d}} = \mathbf{J}^{-1}\mathbf{u}_t = -\mathbf{f}$, cf. Günther [20]. By inserting this into Eq. (57), we obtain:

$$\tilde{\mathbf{u}}^* = \mathbf{0} \quad \text{for} \quad \mathbf{u} - \mathbf{f} + r\mathbf{g} = \mathbf{0}. \tag{59}$$

which is the vortex criterion that was reported by Günther and Theisel [25]. Thus, our general method includes Galilean invariance as a special case.

REFERENCES

[1] G. Astarita. Objective and generally applicable criteria for flow classification. *Journal of Non-Newtonian Fluid Mechanics*, 6(1):69–76, 1979.

[2] V. C. Azevedo, C. Batty, and M. M. Oliveira. Preserving geometry and topology for fluid flows with thin obstacles and narrow gaps. *ACM Trans. Graph.*, 35(4):97:1–97:12, July 2016. doi: 10.1145/2897824.2925919

[3] I. Baeza Rojo, M. Gross, and T. Günther. Visualizing the phase space of heterogeneous inertial particles in 2D flows. *Computer Graphics Forum (Proc. EuroVis)*, p. to appear, 2018.

[4] D. Bauer and R. Peikert. Vortex tracking in scale-space. In *Proc. Symposium on Data Visualisation*, pp. 233–240, 2002.

[5] J. Bec, L. Biferale, M. Cencini, A. S. Lanotte, and F. Toschi. Spatial and velocity statistics of inertial particles in turbulent flows. *Journal of Physics: Conference Series*, 333(1):012003, 2011.

[6] H. Bhatia, V. Pascucci, R. M. Kirby, and P.-T. Bremer. Extracting features from time-dependent vector fields using internal reference frames. *Computer Graphics Forum (Proc. EuroVis)*, 33(3):21–30, 2014.

[7] R. Bordás. *Optical measurements in disperse two-phase flows: Application to rain formation in cumulus clouds*. PhD thesis, University of Magdeburg, 2011.

[8] J. Brackbill, D. Kothe, and H. Ruppel. Flip: A low-dissipation, particle-in-cell method for fluid flow. *Computer Physics Communications*, 48(1):25 – 38, 1988. doi: 10.1016/0010-4655(88)90020-3

[9] S. Camarri, M.-V. Salvetti, M. Buffoni, and A. Iollo. Simulation of the three-dimensional flow around a square cylinder between parallel walls at moderate Reynolds numbers. In *XVII Congresso di Meccanica Teorica ed Applicata*, 2005.

[10] C. M. Casciola, P. Gualtieri, F. Picano, G. Sardina, and G. Troiani. Dynamics of inertial particles in free jets. *Physica Scripta*, 2010(T142):014001, 2010.

[11] M. S. Chong, A. E. Perry, and B. J. Cantwell. A general classification of three-dimensional flow fields. *Physics of Fluids A: Fluid Dynamics*, 2(5):765–777, 1990.

[12] C. Crowe, M. Sommerfield, and Y. Tsuji. *Multiphase Flows with Droplets and Particles*. CRC Press, 1998.

[13] E. Dresselhaus and M. Tabor. The kinematics of stretching and alignment of material elements in general flow fields. *Journal of Fluid Mechanics*, 236:415–444, 1992.

[14] R. Drouot and M. Lucius. Approximation du second ordre de la loi de comportement des fluides simples. lois classiques déduites de lintroduction dun nouveau tenseur objectif. *Archiwum Mechaniki Stosowanej*, 28(2):189–198, 1976.

[15] M. Farazmand and G. Haller. The Maxey–Riley equation: Existence, uniqueness and regularity of solutions. *Nonlinear Analysis: Real World Applications*, 22:98–106, 2015. doi: 10.1016/j.nonrwa.2014.08.002

[16] R. Fuchs, R. Peikert, H. Hauser, F. Sadlo, and P. Muigg. Parallel Vectors Criteria for Unsteady Flow Vortices. *IEEE Transactions on Visualization and Computer Graphics*, 14(3):615–626, 2008.

[17] D. Garaboa-Paz and V. Pérez-Muñuzuri. A method to calculate finite-time Lyapunov exponents for inertial particles in incompressible flows. *Nonlin. Proc. in Geophys.*, 22(5):571–577, 2015.

[18] C. Garth, R. S. Laramee, X. Tricoche, J. Schneider, and H. Hagen. Extraction and visualization of swirl and tumble motion from engine simulation data. In *Topology-based Methods in Visualization*, Visualization and Mathematics, pp. 121–135. Springer Berlin Heidelberg, 2007.

[19] A. Globus, C. Levit, and T. Lasinski. A tool for visualizing the topology of three-dimensional vector fields. In *Proc. IEEE Visualization*, pp. 33–40, 1991.

[20] T. Günther. *Opacity Optimization and Inertial Particles in Flow Visualization*. PhD thesis, University of Magdeburg, June 2016.

[21] T. Günther and M. Gross. Flow-induced inertial steady vector field topology. *Computer Graphics Forum (Proc. Eurographics)*, 36(2):143–152, 2017.

[22] T. Günther, M. Gross, and H. Theisel. Generic objective vortices for flow visualization. *ACM Transactions on Graphics (Proc. SIGGRAPH)*, 36(4):141:1–141:11, 2017.

[23] T. Günther, A. Kuhn, B. Kutz, and H. Theisel. Mass-dependent integral curves in unsteady vector fields. *Computer Graphics Forum (Proc. EuroVis)*, 32(3):211–220, 2013.

[24] T. Günther, M. Schulze, and H. Theisel. Rotation invariant vortices for flow visualization. *IEEE Transactions on Visualization and Computer Graphics (Proc. IEEE SciVis 2015)*, 22(1):817–826, 2016.

[25] T. Günther and H. Theisel. Vortex cores of inertial particles. *IEEE Transactions on Visualization and Computer Graphics (Proc. IEEE SciVis)*, 20(12):2535–2544, 2014.

[26] T. Günther and H. Theisel. Finite-time mass separation for comparative visualizations of inertial particles. *Computer Graphics Forum (Proc. EuroVis)*, 34(3):471–480, 2015.

[27] T. Günther and H. Theisel. Inertial steady 2D vector field topology. *Computer Graphics Forum (Proc. Eurographics)*, 35(2):455–466, 2016.

[28] T. Günther and H. Theisel. Singularities of the inertial flow map gradient. *Proc. Vision, Modeling, and Visualization (VMV)*, pp. 69–76, 2016.

[29] T. Günther and H. Theisel. Source inversion by forward integration in inertial flows. *Computer Graphics Forum (Proc. EuroVis)*, 35(3):371–380, 2016.

[30] T. Günther and H. Theisel. Backward finite-time Lyapunov exponents in inertial flows. *IEEE Transactions on Visualization and Computer Graphics (Proc. IEEE SciVis 2016)*, 23(1):970–979, 2017.

[31] T. Günther and H. Theisel. The state of the art in vortex extraction. *Computer Graphics Forum*, p. to appear, 2018.

[32] G. Haller. An objective definition of a vortex. *Journal of Fluid Mechanics*, 525:1–26, 2005.

[33] G. Haller, A. Hadjighasem, M. Farazmand, and F. Huhn. Defining coherent vortices objectively from the vorticity. *Journal of Fluid Mechanics*, 795:136–173, 2016.

[34] G. Haller and T. Sapsis. Where do inertial particles go in fluid flows? *Physica D: Nonlinear Phenomena*, 237:573–583, May 2008. doi: 10.1016/j.physd.2007.09.027

[35] J. L. Helman and L. Hesselink. Representation and display of vector field topology in fluid flow data sets. *Computer*, 22(8):27–36, 1989.

[36] J. Hoschek and D. Lasser. *Fundamentals of Computer Aided Geometric Design*. AK Peters, 1993.

[37] J. C. R. Hunt. Vorticity and vortex dynamics in complex turbulent flows. *Transactions on Canadian Society for Mechanical Engineering (Proc. CANCAM)*, 11(1):21–35, 1987.

[38] J. Jeong and F. Hussain. On the identification of a vortex. *Journal of Fluid Mechanics*, 285:69–94, 1995.

[39] D. M. Karl. A sea of change: Biogeochemical variability in the north pacific subtropical gyre. *Ecosystems*, 2(3):181–214, May 1999. doi: 10.1007/s100219900068

[40] D. Kenwright and R. Haimes. Vortex identification – Applications in aerodynamics: A case study. In *Proceedings of the 8th Conference on Visualization '97*, VIS '97, pp. 413–ff. IEEE Computer Society Press, Los Alamitos, CA, USA, 1997.

[41] G. L. Kindlmann, C. Chiw, T. Huynh, A. Gyulassy, J. Reppy, and P.-T. Bremer. Rendering and extracting extremal features in 3D fields. *Computer Graphics Forum*, p. to appear, 2018. doi: 10.1111/cgf.13439

[42] B. M. Kutz, T. Günther, A. Rumpf, and A. Kuhn. Numerical examination of a model rotor in brownout conditions. In *Proceedings of the American Helicopter Society*, number AHS2014-000343, 2014.

[43] H. J. Lugt. The dilemma of defining a vortex. In *Recent developments in theoretical and experimental fluid mechanics*, pp. 309–321. Springer, 1979.

[44] R. S. Martins, A. S. Pereira, G. Mompean, L. Thais, and R. L. Thompson. An objective perspective for classic flow classification criteria. *Comptes Rendus Mecanique*, 344:52–59, Jan. 2016. doi: 10.1016/j.crme.2015.08.002

[45] M. R. Maxey and J. J. Riley. Equation of motion for a small rigid sphere in a nonuniform flow. *Physics of Fluids*, 26(4):883–889, 1983.

[46] H. Miura and S. Kida. Identification of tubular vortices in turbulence. *Journal of the Physical Society of Japan*, 66(5):1331–1334, 1997.

[47] A. Okubo. Horizontal dispersion of floatable particles in the vicinity of velocity singularities such as convergences. *Deep Sea Research and Oceanographic Abstracts*, 17(3):445–454, 1970.

[48] T. Oster, C. Rössl, and H. Theisel. Core lines in 3d second-order tensor fields. *Computer Graphics Forum (Proc. EuroVis 2018)*, p. to appear, 2018.

[49] R. Peikert and M. Roth. The "parallel vectors" operator – a vector field visualization primitive. In *Proc. IEEE Visualization*, pp. 263–270, 1999.

[50] J. Peng and J. O. Dabiri. Transport of inertial particles by Lagrangian coherent structures: Application to predator–prey interaction in jellyfish feeding. *Journal of Fluid Mechanics*, 623:75–84, 3 2009. doi: 10.1017/S0022112008005089

[51] F. Picano, G. Sardina, P. Gualtieri, and C. Casciola. DNS of a free turbulent jet laden with small inertial particles. In H. Kuerten, B. Geurts, V. Armenio,

and J. Fröhlich, eds., *Direct and Large-Eddy Simulation VIII*, vol. 15 of *ERCOFTAC Series*, pp. 189–194. Springer Netherlands, 2011. doi: 10.1007/978-94-007-2482-2_30

[52] S. Popinet. Free computational fluid dynamics. *Cluster World 2*, (6), 2004.

[53] S. K. Robinson. Coherent motions in the turbulent boundary layer. *Annual Review of Fluid Mechanics*, 23(1):601–639, 1991.

[54] A. Rockwood, K. Heaton, and T. Davis. Real-time rendering of trimmed surfaces. In *ACM SIGGRAPH Computer Graphics*, vol. 23, pp. 107–116. ACM, 1989.

[55] S. Roettger, M. Schulz, W. Bartelheimer, and T. Ertl. Automotive soiling simulation based on massive particle tracing. In *Data Visualization 2001*, Eurographics, pp. 309–317. Springer Vienna, 2001. doi: 10.1007/978-3-7091-6215-6_33

[56] M. Roth and R. Peikert. A higher-order method for finding vortex core lines. In *Proc. IEEE Visualization*, pp. 143–150, 1998.

[57] A. Sagristà, S. Jordan, A. Just, F. Dias, L. G. Nonato, and F. Sadlo. Topological analysis of inertial dynamics. *IEEE Transactions on Visualization and Computer Graphics (Proc. IEEE SciVis 2016)*, 23(1):950–959, 2017.

[58] J. Sahner, T. Weinkauf, and H.-C. Hege. Galilean invariant extraction and iconic representation of vortex core lines. In *Proc. Eurographics / IEEE VGTC Symposium on Visualization (EuroVis)*, pp. 151–160, 2005.

[59] J. Sahner, T. Weinkauf, N. Teuber, and H.-C. Hege. Vortex and strain skeletons in Eulerian and Lagrangian frames. *IEEE Transactions on Visualization and Computer Graphics*, 13(5):980–990, 2007.

[60] T. Sapsis, J. Peng, and G. Haller. Instabilities on prey dynamics in jellyfish feeding. *Bull Math Biol.*, 73(8):1841–1856, 2011.

[61] T. P. Sapsis and G. Haller. Inertial particle dynamics in a hurricane. *Journal of the Atmospheric Sciences*, 66(8):2481–2492, 2009.

[62] S. Schaefer, J. Hakenberg, and J. Warren. Smooth subdivision of tetrahedral meshes. In *Proceedings of the 2004 Eurographics/ACM SIGGRAPH Symposium on Geometry Processing*, SGP '04, pp. 147–154. ACM, New York, NY, USA, 2004. doi: 10.1145/1057432.1057452

[63] T. Schafhitzel, J. Vollrath, J. Gois, D. Weiskopf, A. Castelo, and T. Ertl. Topology-preserving lambda2-based vortex core line detection for flow visualization. *Computer Graphics Forum (Proc. EuroVis)*, 27(3):1023–1030, 2008.

[64] Y. Shao and A. Li. Numerical modelling of saltation in the atmospheric surface layer. *Boundary-Layer Meteor.*, 91:199–225, 1999. doi: 10.1023/A:1001816013475

[65] C. R. Short, D. Blazevski, K. C. Howell, and G. Haller. Stretching in phase space and applications in general nonautonomous multi-body problems. *Celestial Mechanics and Dynamical Astronomy*, 122:213–238, 2015. doi: 10.1007/s10569-015-9617-4

[66] D. Stalling, M. Westerhoff, and H.-C. Hege. Amira: A highly interactive system for visual data analysis. In *The Visualization Handbook*, pp. 749–767. Elsevier, 2005.

[67] R. C. Strawn, D. N. Kenwright, and J. Ahmad. Computer visualization of vortex wake systems. *AIAA journal*, 37(4):511–512, 1999.

[68] M. Sudharsan, S. L. Brunton, and J. J. Riley. Lagrangian coherent structures and inertial particle dynamics. *ArXiv e-prints*, 2015. 1512.05733.

[69] D. Sujudi and R. Haimes. Identification of swirling flow in 3D vector fields. Technical report, Departement of Aeronautics and Astronautics, MIT, 1995. AIAA Paper 95-1715.

[70] M. Syal, B. Govindarajan, and J. G. Leishman. Mesoscale sediment tracking methodology to analyze brownout cloud developments. In *Proceedings of the American Helicopter Society, 66th Annual Forum*, 2010.

[71] A. Sydney, A. Baharani, and J. G. Leishman. Understanding brownout using near-wall dual-phase flow measurements. In *Proceedings of the American Helicopter Society*, 67th Annual Forum. Virginia Beach, VA, May 2011.

[72] M. Tabor and I. Klapper. Stretching and alignment in chaotic and turbulent flows. *Chaos, Solitons & Fractals*, 4(6):1031–1055, 1994.

[73] H. Theisel, J. Sahner, T. Weinkauf, H.-C. Hege, and H.-P. Seidel. Extraction of parallel vector surfaces in 3D time-dependent fields and application to vortex core line tracking. In *Proc. IEEE Visualization*, pp. 631–638, 2005.

[74] H. Theisel and H.-P. Seidel. Feature flow fields. In *Proc. Symposium on Data Visualisation*, pp. 141–148, 2003.

[75] R. L. Thompson. Some perspectives on the dynamic history of a material element. *International Journal of Engineering Science*, 46(3):224–249, 2008.

[76] X. Tricoche, T. Wischgoll, G. Scheuermann, and H. Hagen. Topology tracking for the visualization of time-dependent two-dimensional flows. *Computers & Graphics*, 26(2):249–257, 2002.

[77] C. Truesdell and W. Noll. *The nonlinear field theories of mechanics*. Handbuch der Physik, Band III/3, e by Flugge, S., (ed.) , Springer-Verlag, Berlin, 1965.

[78] A. Van Gelder and A. Pang. Using PVsolve to analyze and locate positions of parallel vectors. *IEEE Transactions on Visualization and Computer Graphics*, 15(4):682–695, 2009. doi: 10.1109/TVCG.2009.11

[79] T. Weinkauf, J. Sahner, H. Theisel, and H.-C. Hege. Cores of swirling particle motion in unsteady flows. *IEEE Transactions on Visualization and Computer Graphics (Proc. Visualization)*, 13(6):1759–1766, 2007.

[80] J. Weiss. The dynamics of enstrophy transfer in two-dimensional hydrodynamics. *Physica D: Nonlinear Phenomena*, 48(2-3):273–294, 1991.

[81] J. Zhou, R. J. Adrian, S. Balachandar, and T. M. Kendall. Mechanisms for generating coherent packets of hairpin vortices in channel flow. *Journal of Fluid Mechanics*, 387:353–396, 1999.